Available online at www.sciencedirect.com
SCIENCE DIRECT®
Physics of the Earth and Planetary Interiors 141 (2004) 253–267
PHYSICS OF THE EARTH AND PLANETARY INTERIORS
www.elsevier.com/locate/pepi

Stresses along the metastable wedge of olivine in a subducting slab: possible explanation for the Tonga double seismic layer

A. Guest [a,c,*], G. Schubert [a], C.W. Gable [b]

[a] *Department of Earth and Space Sciences and Institute of Geophysics and Planetary Physics, University of California, Los Angeles, CA 90095, USA*
[b] *Earth and Environmental Sciences Division, Los Alamos National Laboratory, Los Alamos, New Mexico, NM 87545, USA*
[c] *Geophysical Institute, Academy of Science of the Czech Republic, Prague, Czech Republic*

Accepted 24 November 2003

Abstract

A numerical calculation of the stresses associated with changes in volume during phase transitions of olivine in a descending slab results in a double layer of high shear stress along the metastable olivine wedge in the depth range 350–460 km. Stress in the upper layer is in-plane tensional and stress in the lower layer is down-dip compressional. The modeled stress field agrees with observations of stress in the Tonga double seismic zone. High shear stress also exists in the slab at depths below the metastable wedge. This stress distribution involves down-dip compression and trench-parallel tension, which agrees with about half of the focal mechanisms in the Tonga slab at depths of 460–690 km. The model supports the idea that at least two possible stress release mechanisms for deep earthquakes may act in the Tonga subducting slab. One, transformational faulting, is restricted to the metastable wedge while the other one acts below the metastable wedge.

Keywords: Subduction; Stress; Phase transformations; Double seismic zone; Tonga

1. Introduction

A long standing question is whether a metastable wedge of olivine is present in subducting lithosphere. The best indication of a metastable wedge is the observation of hypocenters of earthquakes forming a double seismic layer in the Tonga (Wiens et al., 1993) and Izu-Bonin (Iidaka and Furukawa, 1994) subduction zones. In the Izu-Bonin, the double seismic layer occurs in the depth range 300–400 km, while in northern Tonga it occurs between 380 and 460 km depth and in southern Tonga it occurs in the depth range 350–420 km. The upper seismic zone is less seismically active in southern Tonga. The distance between the seismic layers is about 20–40 km, and the seismic layers merge into one above and below the double seismic region. The along strike width of the double seismic layer is 180–200 km (Wiens et al., 1993). Various seismic methods based on travel times of seismic waves through the subducting slab and the surrounding mantle were used to support the presence of a metastable wedge. Iidaka and Suetsugu (1992), Iidaka and Furukawa (1994), and Iidaka and Obara (1997), and Brudzinski and Chen (2000) support the presence of a metastable wedge in Izu-Bonin, and in Tonga, respectively, whereas Collier et al. (2001), and Koper et al. (1998) and Chen and Brudzinski (2001) deny the existence of a metastable wedge in

* Corresponding author.
E-mail addresses: alickaguest@yahoo.com (A. Guest), schubert@ucla.edu (G. Schubert), gable@lanl.gov (C.W. Gable).

0031-9201/$ – see front matter © 2004 Elsevier B.V. All rights reserved.
doi:10.1016/j.pepi.2003.11.012

northwest Pacific subduction zones, and in Tonga, respectively.

Seismic observations in the Tonga subduction zone allow for the determination of focal mechanisms, that reflect the state of stress in the double seismic layer. The upper layer is in-plane tensional whereas the lower layer is in-plane compressional (Wiens et al., 1993). The Tonga subduction zone is seismically active from the surface to a depth of 690 km, whereas the double seismic layer is observed approximately in the depth range 350–460 km. The characteristic of Tonga seismic activity from Harvard Centroid Moment Tensor (HCMT) is that the P axes are oriented close to the down-dip direction throughout the slab from 100 km depth to the bottom of the seismic zone. Since the double seismic layer is not observed along the whole strike of the subduction zone, focal mechanisms from the lower layer prevail in global seismic data set. Down to about 450 km depth, B axes are parallel to the trench and T axes are perpendicular to the slab plane. Below 450 km depth, T and B axes become interchangeable, which means that the magnitude of the stresses in these directions are nearly equal (Jiao et al., 2000). The change of focal mechanism may be related to a change in the mechanism of failure for deep earthquakes. Transformational faulting (related to the metastability of olivine, Green and Burnley, 1989; Kirby et al., 1991) can be active at depths shallower than 450 km and another failure mechanism may be active deeper than 450 km depth.

In this paper we present a numerical model of stress associated with mineral metastability in the subducting lithosphere. Our goals are to model the state of stress in the subducting slab, compare it to the focal mechanisms and seismic activity in the Tonga subduction zone, estimate whether the stress field around the metastable wedge can produce a double seismic layer (as it was suggested by Bina (1996) and Yoshioka et al. (1997)), and estimate whether the stress field below the metastable wedge fits the seismic observations. Since it has been found that buoyancy forces do not produce a double shear layer along a metastable wedge (Goto et al., 1985; Bina, 1997; Yoshioka et al., 1997), we focus our attention on the effects of volumetric strains due to the change of density in the slab (Goto et al., 1983, 1987; Devaux et al., 2000; Guest et al., 2003). In our model, the lithosphere is composed of olivine and its high-pressure phases. The heat conduction equation is solved in the slab to determine temperature conditions in the slab and locate the phase transitions in pressure-temperature space. Volumetric strains in the subducting lithosphere are calculated from the density of individual phases and the heat released or consumed in the phase changes. These strains are used as sources of stress in the subducting lithosphere. Dislocation creep, diffusion creep and Peierls stress creep laws are included in the viscoelastic rheology (Devaux et al., 1997, 2000; Guest et al., 2003).

2. Model description

The geometry of the subducting lithosphere is approximated by a two-dimensional structure (Fig. 1). The slab of thickness ‘De’ descends into the mantle with a velocity v at an angle δ to the horizontal (Table 1).

The approach to the modeling is the same as in Devaux et al. (1997, 2000) and Slancova et al. (2002). A short description follows.

2.1. Momentum and rheological equations

The balance of forces is expressed by the equation

$$\frac{\partial \sigma_{ij}}{\partial x_j} + f_i = 0, \quad i = 1, 2, 3 \tag{1}$$

where σ_{ij} is the stress tensor and f_i is the sum of the body forces acting on the slab. The x_i are the Cartesian

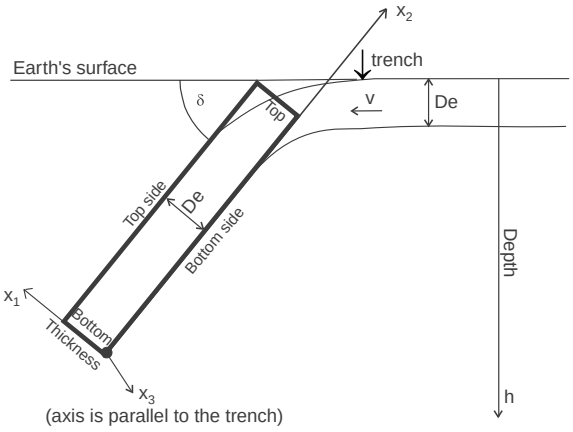

Fig. 1. Sketch of the slab model.

Table 1
Model parameters

Name	Value
Velocity, v (mm per year)	100
Dip angle, δ (°)	50
Gravity acceleration, g ($m\,s^{-2}$)	9.8
Thickness of the lithosphere, De (km)	95
Temperature at the base of the lithosphere, T_l (K)	1473 (cold)[a]; 1723 (hot)[a]
Adiabatic gradient in the mantle ($K\,km^{-1}$)	0.3[b]
Slab density, ρ ($kg\,m^{-3}$)	3300[b]
Specific heat, c_p ($J\,kg^{-1}\,K^{-1}$)	1.05×10^{-5}[c]
Thermal conductivity, k ($W\,m^{-1}\,K^{-1}$)	3.465[b]
First-order thermal expansivity, α_0 (K^{-1})	3×10^{-5}[b]
Second-order thermal expansivity, α_1 ($K^{-1}\,m^{-1}$)	2×10^{-11}[b]

[a] Stein and Stein (1992).
[b] Turcotte and Schubert (1982).
[c] Devaux et al. (1997).

coordinates described in Fig. 1. The stress σ_{ij} does not include the hydrostatic pressure of the surrounding mantle. The body forces f_i thus include the buoyancy forces due to the difference of density between a given point inside the slab and a point at the same depth far from the slab. In our calculations, we put $f_i = 0$, because we assume that the gravitational torque applied to the slab is balanced by the lifting pressure torque (Turcotte and Schubert, 1982). This balance sets the constant dip of the lithosphere. When the dip of the lithosphere remains constant, the stress due to buoyancy forces is at least one order of magnitude less than the stresses due to phase change induced volume changes (Devaux et al., 2000, elastic case).

We use the constitutive relation of a Maxwell body to describe the viscoelastic behavior

$$\dot{\sigma}_{ij} + \frac{\mu}{\nu}(\sigma_{ij} - \tfrac{1}{3}\sigma_{kk}\delta_{ij}) = K\dot{\epsilon}_{kk}\delta_{ij} + 2\mu(\dot{\epsilon}_{ij} - \tfrac{1}{3}\dot{\epsilon}_{kk}\delta_{ij}) - K\dot{\epsilon}^{\mathrm{T}}_{ij}\delta_{ij} - K\dot{\epsilon}^{\mathrm{V}}_{ij}\delta_{ij}, \quad (2)$$

where $\dot{\epsilon}_{ij}$ is the time derivative of the strain tensor ϵ_{ij}

$$\epsilon_{ij} = \frac{1}{2}\left(\frac{\partial u_i}{\partial x_j} + \frac{\partial u_j}{\partial x_i}\right), \quad (3)$$

u_i is the displacement of a point at time t from its initial position in our reference frame, K is the bulk modulus, μ is the shear modulus, ν is the viscosity, and δ_{ij} is the Kronecker delta. $\dot{\epsilon}^{\mathrm{T}}_{ij}$ and $\dot{\epsilon}^{\mathrm{V}}_{ij}$ are the strain rates inside the slab due to thermal expansion from the warming of the slab and volume contraction due to phase transitions

$$\dot{\epsilon}^{\mathrm{T}}_{ij} = \tfrac{1}{3}\alpha\delta_{ij}\dot{T} \quad (4)$$

$$\dot{\epsilon}^{\mathrm{V}}_{ij} = -\frac{1}{3}\left(\frac{\dot{\rho}}{\Delta\rho}\right)\delta_{ij} \quad (5)$$

In (4), α is the coefficient of thermal expansion and $\dot{T}$ is the time derivative of the temperature for the individual lagrangian points of the model during the individual time steps. Similarly in (5), ρ is density, $\Delta\rho$ is the positive density difference between the high-pressure phase and the low-pressure phase, and $(\dot{\rho}/\Delta\rho)$ is the time derivative of the fractional volume change of a phase transition. We assume that the volume changes across the phase boundaries are isotropic (Goto et al., 1983, 1985; Devaux et al., 2000). Parameter values are listed in Table 2 and are discussed in detail below.

2.2. Boundary conditions

The boundary conditions on the bottom side ($x_1 = 0$), on the top side ($x_1 = \mathrm{De}$), and on the leading edge of the slab bottom ($x_2 = 0$) are chosen to be stress free so that only the pressure in the mantle acts on these boundaries. The top of the slab is pinned ($u_i = 0$) at the trench. We used zero displacement ($u_3 = 0$, plane strain) boundary condition in the direction parallel to the trench axis.

2.3. Numerical analysis

Eqs. (1)–(5) applied to a two-dimensional structure form a system of two coupled equations with unknowns u_1 and u_2. The equations are solved using a staggered-grid finite difference technique (Madariaga, 1976) with staggered u_1 and u_2 variables. We use a 2 km grid spacing in the x_1 and x_2 directions. The numerical code was tested against analytic solutions of several problems (elastic deformation of a slab by its own weight, elastic deformation of a slab in tension, viscoelastic deformation of a uniformly loaded slab supported on one side). We also performed a number of numerical tests for cases with spatially-dependent physical parameters and compared them against the numerical results of Devaux et al. (2000).

Table 2
Elastic and creep parameters

Parameters	α	β	γ	pv	MgO
Molar volume, V_m ($cm^3\,mol^{-1}$)	43.67	40.52	39.66	24.46	11.25
Density, ρ_0 ($kg\,m^{-3}$)	3222[a]	3473[a]	3548[a]	4104[b]	3583[b]
Bulk modulus, K (GPa)	129[c]	174[c]	184[c]	261[d]	164[e]
Shear modulus, μ (GPa)	82[e]	114[f]	119[g]	184[h]	132[e]
Thermal expansivity, α ($10^{-5}\,K^{-1}$)	3.05[i]	2.71[i]	2.37[i]	1.73[d]	3.12[e]
Grüeisen parameter, γ (1)	1.25[c]	1.30[c]	1.35[c]	1.96[j]	1.54[e]
Power n for dislocation creep (1)	3.5[k]	3.5[l]	3.5[k]	3.0[m]	3.3[n]
Pre-exponential coefficient for dislocation creep, C_1 ($Pa^{-n}\,s^{-1}$)	$\frac{3.5\times10^{22}}{\mu^n(p,T)}$[k]	$\frac{4.0\times10^{22}}{\mu^n(p,T)}$[l]	$\frac{4.0\times10^{22}}{\mu^n(p,T)}$[k]	2.1186×10^{9}[m]	$\frac{10^{24}}{1.381T}b\mu(p,T)^{(1-n)}$[n]; $b=2.28\times10^{-10}\exp\left(\frac{p}{3K_0}\right)$
Pre-exponential coefficient for Peirls's law, C_2 ($10^{11}\,s^{-1}$)	5.7[o]	7.0[l]	7.0[k]	–	–
Peierl's stress, σ_P (GPa)	8.5[o]	10[l]	10[k]	–	–
Constant, g_m proportional to activation energy (1)	31[k]	31[l]	31[k]	20.8[m]	10.3[n]
Pressure dependenee of melting temperature $T_m(p)$ (K)					
α	$T_m(p)=2171\left(1+\frac{p}{2.44}\right)^{1/11.4}$[p]				
β	$T_m(p)=46.38p+1833.15$[q]				
γ	$T_m(p)=46.38p+1833.15$[q]				
pv	$T_m(p)=26.695p+2572.5$[r]				
MgO	$T_m(p)=-0.539p^2+52.15p+3043.63$[s]				
Pre-exponential coefficient for diffusion creep, C_3 ($10^{-14}\,s^{-1}\,m^2\,Pa^{-1}$)	–	2.34[t]	2.34[t]	–	–
Activation energy for diffusion, Q_d ($10^3\,J\,mol^{-1}$)	–	296[t]	296[t]	–	–
Activation volume for diffusion, V_a ($10^{-6}\,m^3\,mol^{-1}$)	–	5.33[t]	5.33[t]	–	–
Original grain size, $d(0)$ (10^{-3} m)	1	–	–	–	–

[a] Jeanloz and Thompson (1983).
[b] Duffy and Anderson (1989).
[c] Akaogi et al. (1987).
[d] Yusa et al. (1993).
[e] Anderson and Isaak (1995).
[f] Sawamoto et al. (1984).
[g] Weidner et al. (1984).
[h] Yeganeh-Haeri et al. (1989).
[i] Akaogi et al. (1989).
[j] Stixrude et al. (1992).
[k] Karato et al. (2001).
[l] Assumed to be the same as for γ.
[m] Wright et al. (1992).
[n] Frost and Ashby (1982).
[o] Goetze and Evans (1979).
[p] Presnell and Walter (1993).
[q] $T_m(p)$ is linearly interpolated between two points: (1) $T_m(p)$ of α-olivine at pressure of α to β reaction and (2) $T_m(p)$ of perovskite at pressure of γ to $pv+$MgO reaction.
[r] Wang (1999).
[s] Zerr and Boehler (1994).
[t] Riedel and Karato (1997).

2.4. Temperature

The temperature distribution inside the slab is computed using the heat conduction equation:

$$\rho c_p \frac{\partial T}{\partial t} = k\left(\frac{\partial^2 T}{\partial x_1^2} + \frac{\partial^2 T}{\partial x_2^2}\right) + \rho v \alpha g T \sin\delta + Q_L \quad (6)$$

in which adiabatic heating (second term on the right side) and latent heat Q_L released or absorbed during phase transitions of minerals are included (determined by (12)). We consider the convective term to be negligible. The specific heat at constant pressure is c_p, t is the time, and k is the thermal conductivity. The coefficient of volume expansion α is assumed to be only a function of the depth h

$$\alpha = \alpha_0 - \alpha_1 h \quad (7)$$

The adiabatic temperature profile in the mantle is used as a boundary condition on the temperature in the slab and the distribution of temperature in the oceanic lithosphere before subduction is used as an initial condition (Fig. 2, Table 1)

$$T(x_1, t=0) = (T_l - 273\,\mathrm{K})\left(1 - \frac{x_1}{\mathrm{De}}\right) + 273\,\mathrm{K} \quad (8)$$

where T_l is the temperature at the base of lithosphere at the onset of subduction. An adiabatic temperature gradient of $0.3\,\mathrm{K\,km^{-1}}$ was used in both temperature models (Turcotte and Schubert, 1982), while the basal temperature was 1473 K for the 'cold' model and 1723 K for the 'hot' model (Stein and Stein, 1992) (Fig. 2).

2.5. Pressure

The model PREM (Dziewonski and Anderson, 1981) is used to convert pressure into depth.

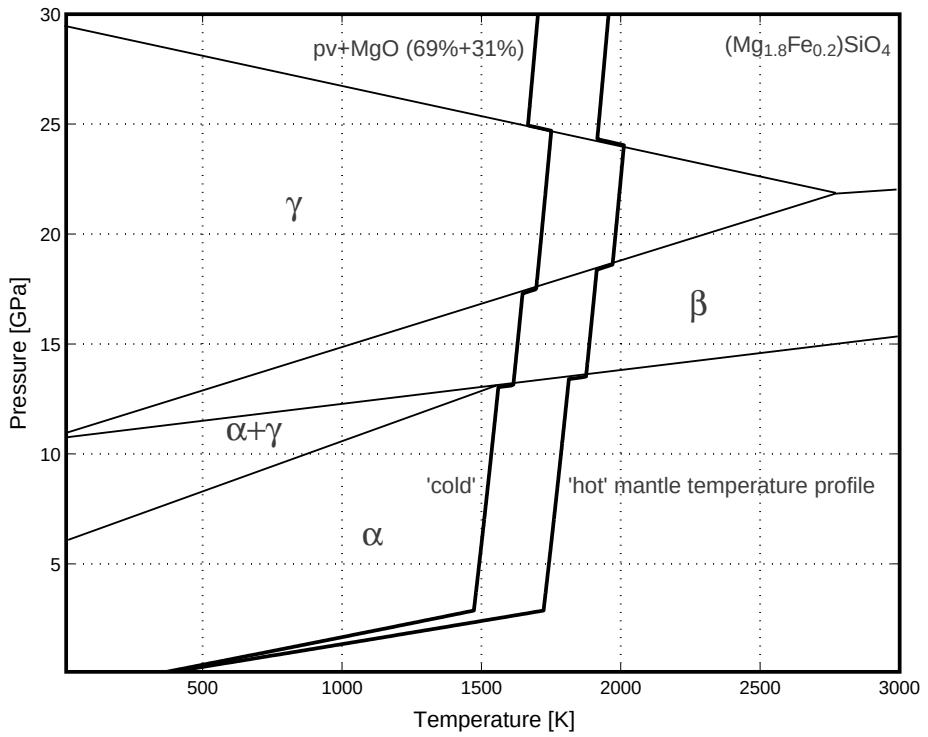

Fig. 2. Phase diagram of $(Mg_{1.8}Fe_{0.2})SiO_4$ (thin solid lines) and mantle temperature profiles (thick solid lines) used as boundary conditions for the heat equation. Two mantle temperature models are tested. The 'cold' model uses 1473 K as the temperature at the base of the lithosphere. The 'hot' model uses 1723 K. The thickness of the lithosphere is 95 km. The adiabatic gradient is $0.3\,\mathrm{K\,km^{-1}}$ in both models. The jumps in the temperature gradient are caused by latent heat released or consumed during phase transformations.

2.6. Mineralogical composition

The major minerals in the subducting lithosphere are olivine, pyroxene and garnet and their high-pressure equivalents (Ringwood, 1982). We assume a simplified mineralogical composition of the subducting slab simulating phase transitions of $(Mg_{1.8}, Fe_{0.2})SiO_4$-olivine ($\alpha$) to $\alpha+\gamma$, $\alpha+\beta$, β, $\beta+\gamma$ and γ phases and the dissociation of γ-spinel to perovskite and magnesiowüstite (Akaogi et al., 1989). This phase sequence is simplified to α to β, γ and dissociation to perovskite and magnesiowüstite, similarly to Kirby et al. (1996). In contrast to Kirby et al. (1996), we add the phase field $\alpha+\gamma$ as a univariant phase boundary (Fig. 2), because we seek to determine the minimum depth where the effect of the phase change can be observed. The model we use is similar to the simple model where pure $(Mg)_2SiO_4$-olivine is considered; the only difference is in the depth location of phase boundaries. These need to be better located since we compare the model with seismic observations. As will be seen later, consideration of the $\alpha+\gamma$ phase shifts the depth location of shear stress along the metastable boundary to a shallower depth. The orientation of the principal stress axes remains the same, whereas the magnitude of the shear stress depends on the volume of a transformed phase (e.g. 10% γ in $\alpha+\gamma$) and the viscosity of the newly transformed phase. Accordingly, the assumed composition of the slab is adequate for the study of the stress field along the metastable wedge and its comparison with focal mechanisms, mainly because the magnitude of the stress drop during the deep earthquakes is not known. A model that would include the complex mineral and chemical composition of a real slab should be studied in the future.

We consider metastability of the α to $\alpha+\gamma$ and $\alpha+\gamma$ to β phase transformations. We use the following kinetic relations (Cahn, 1956; Rubie and Ross, 1994; Daessler et al., 1996; Devaux et al., 1997):

$$\xi(t) = 1 - \exp\left(-\frac{6.7}{d}\int_0^\infty [1-\exp(-Y_e(y,t))]\,dy\right) \tag{9}$$

$$Y_e(y,t) = \pi\int_0^t I\left[\left(\int_\tau^t Y\,d_r t'\right)^2 - y^2\right]d\tau, \tag{10}$$

where ξ is the degree of transition, $0 \le \xi \le 1$, I is the nucleation rate, Y is the growth rate, and d_r is the diameter of the reactant grain. The parameter values are taken from Devaux et al. (1997). We assume that kinetic parameters are the same for the α to β and α to γ transformations and that only the Gibbs free energy change of reaction differs (Rubie and Ross, 1994). The free energy change for the reactions is expressed by

$$0 = (p - P_0)\Delta V - T\,\Delta S. \tag{11}$$

where the parameter P_0, the change of entropy ΔS and the change of volume ΔV of appropriate phase reactions are listed in Table 3 . The β to γ and γ to perovskite + magnesiowüstite phase transitions were modeled using (11). The model of the stress field associated with the equilibrium phase transitions is described in detail in Slancova et al. (2002).

The latent heat Q_L from (6) is related to the degree of phase transition (Devaux et al., 1997):

$$Q_L = \frac{\partial\xi}{\partial t}\frac{(p-P_0)\Delta V}{V_m} \tag{12}$$

where V_m is molar volume of a mineral phase.

2.7. Elastic constants and density

The values of elastic parameters K and μ and densities ρ at given p–T conditions are calculated from the same equations as in Goto et al. (1983) or Devaux et al. (2000). The parameters are listed in Slancova et al. (2002).

Table 3
Thermodynamic parameters

Parameters	α to β	α to $\alpha+\gamma$	β to γ	γ to $pv+MgO$
Volume change of reaction, ΔV ($cm^3\,mol^{-1}$)	−3.16	−0.414	−0.98	−2.59
Entropy change of reaction, ΔS ($J\,mol^{-1}\,K^{-1}$)	−5.02	−1.895	−4.10	7.25
Reference pressure, P_0 at $T = 0$ K (GPa)	10.558	5.87	10.640	29.360

Fit to Clapeyron curve in p–T space of Fig. 6 in Kirby et al. (1996).

2.8. Viscosity

We consider the dislocation creep, diffusion creep and Peierls stress creep laws.

The relation for viscosity is:

$$\nu = \frac{\sigma}{2\dot{\epsilon}} \tag{13}$$

where σ is the square root of the second invariant of the deviatoric stress and $\dot{\epsilon}$ is a strain rate determined as a sum of the dislocation creep (Frost and Ashby, 1982; Karato et al., 2001):

$$\dot{\epsilon}_1 = C_1 \sigma^n \exp\left(\frac{-g_m T_m(p)}{T}\right), \tag{14}$$

the Peierls stress law (Karato et al., 2001):

$$\dot{\epsilon}_2 = C_2 \exp\left[\frac{-g_m T_m(p)}{T}\left(1 - \frac{\sigma}{\sigma_P}\right)^2\right], \tag{15}$$

and the diffusion creep:

$$\dot{\epsilon}_3 = \frac{C_3 \sigma}{d^2} \exp\left(\frac{-(Q_D + pV_a)}{RT}\right), \tag{16}$$

where C_1, C_2 and C_3 are the pre-exponential coefficients, g_m is a constant proportional to creep activation energy, $T_m(p)$ is the pressure-dependent melting temperature of individual minerals (Karato et al., 2001), σ_P is the Peierls stress, d is the grain size, Q_D is an activation energy, V_a is an activation volume, and R is the universal gas constant. Parameter values are given in Table 2. The Peierls stress creep law is not considered for perovskite, because it is not well known, even though the stress dependence of activation energy of creep in perovskite has been reported (Wang et al., 1993). The Peierls stress creep law is also not considered for magnesiowüstite (Frost and Ashby, 1982), because it cannot be used without the Peierls stress creep law for perovskite. The grain size reduction and subsequent grain growth was determined according to Riedel and Karato (1996, 1997) and Karato et al. (2001). The grain size reduction occurs when 10% of the α phase is transformed. The grain then grows according to:

$$d^2(t) - d^2(0) = k_0 \exp\left(\frac{-H_{gg}}{RT}\right) t \tag{17}$$

where $d(t)$ is grain size at time t, $d(0)$ is the original grain size, H_{gg} is the activation energy and k_0 is the pre-exponential factor (Karato et al., 2001). We used the same parameters as in Karato et al. (2001).

We use the fraction of molar volumes in the slab: 0.9 for α and 0.1 for γ (based on the presence of 10% of Fe in olivine) for the $\alpha + \gamma$ stability field, and 0.7 for perovskite and 0.3 for magnesiowüstite for lower mantle minerals. When two phases coexist, the parameters ρ, K, μ and $\dot{\epsilon}$ are weighted according to the degree of phase transformation ξ.

3. Results

Fig. 3 shows the temperature distribution and locations of phase boundaries in the slab for the 'cold' mantle temperature profile. In the coldest part of the slab, about 10% of the α to $\alpha + \gamma$ phase transition is transformed at 500 km depth. The phase transition is completed at 590 km depth. The $\alpha + \gamma$ to β transition is completed at 600 km depth, β to γ at 615 km depth, and γ to perovskite + magnesiowüstite at 725 km depth. Grain size reduction starts during the α to $\alpha + \gamma$ phase transition at 575 km depth in the coldest part of the slab, and around 440 km at the edges of a grain-size-reduction area.

Fig. 4 shows the shear stress distribution in the subducting slab when the 'cold' mantle temperature profile is used. The maximum shear stress (1–1.5 GPa) is concentrated along the phase boundary of the metastable wedge of the $\alpha + \gamma$ to β phase transition and the subsequent β to γ phase transition and thus creates two layers of high shear stress. The outside part of the wedge undergoes contraction that causes tension outside the wedge and down-dip compression inside the wedge. The stress state of upper layer is in-plane tension with a compression perpendicular to the slab plane. The tension occurs in the new phase stability field and is caused by the volume reduction (shrinking) of the new phase. The state of stress is more complex in the lower layer. In the depth range 380–560 km, the highest shear stress is located inside the metastable wedge. The compression is in a down-dip direction, middle axis (the principal stress axes are called: compression, middle axis and tension) is trench parallel and tension is perpendicular to the slab plane. In the depth range 560–615 km, high shear stress is concentrated along the metastable phase boundaries rather than inside

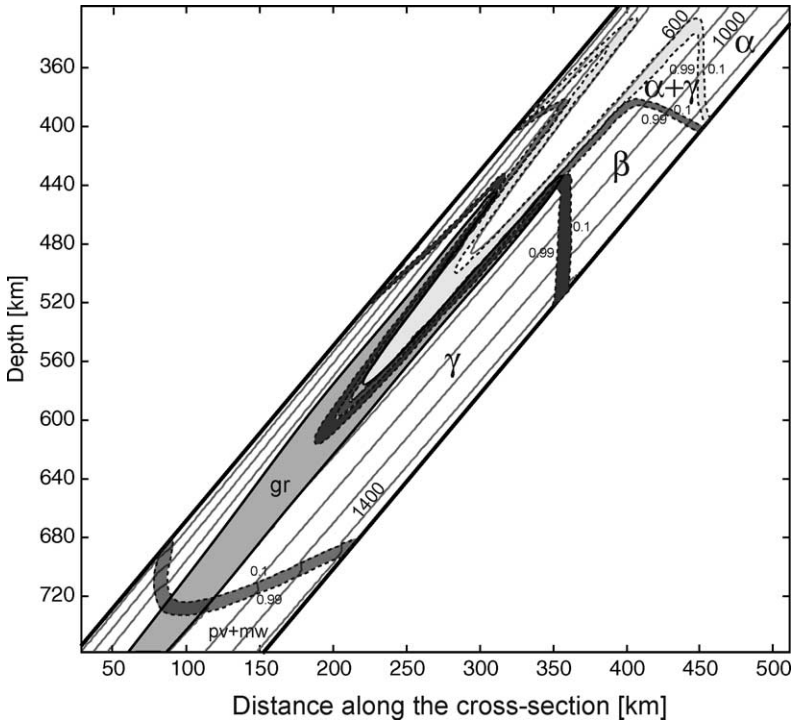

Fig. 3. Temperature (K) distribution (gray solid lines), phase boundaries (dashed lines), and the area of grain size reduction (gray filled area, labeled 'gr', and defined by solid black lines) in the subducting slab. The 'cold' mantle temperature profile was used to determine the temperature distribution inside the slab. Degrees of transformation 0.1 and 0.99 are shown for all phases.

the metastable wedge. Compression is perpendicular to the slab plane, middle axis is in a down-dip direction, and tension is parallel to the trench. Below 615 km depth, after the completion of phase transitions, the orientation of principal stress axes remains the same, and only the magnitude of stress decreases. The shear stress below the equilibrium phase transitions (here β to γ) is caused by the non-uniform distribution of viscosity across the slab (for details see Slancova et al., 2002). The magnitude and orientation of tension along the trench are caused by the boundary condition in the x_3-direction. This boundary condition does not allow any displacement in this direction while at the same time the internal strain forces the slab to shrink. Even though grain size reduction occurs, the resulting viscosity is not low enough to relax all the shear stress inside and below the metastable wedge. The stress below the γ to perovskite + magnesiowüstite phase transition is fully relaxed.

Fig. 5 shows the temperature distribution and location of phase boundaries in the slab for the 'hot' mantle temperature profile. In the coldest part of the slab, about 10% of the α to $\alpha + \gamma$ phase transition is transformed at 360 km depth. The phase transition is completed at 440 km depth. The $\alpha + \gamma$ to β transition is completed at 450 km depth, β to γ at 465 km depth, and γ to perovskite + magnesiowüstite at 730 km depth. Grain size reduction starts during the $\alpha + \gamma$ to β transition at 430–440 km depth.

Fig. 6 shows the shear stress distribution in the subducting slab when the 'hot' mantle temperature profile is used. The stress field is similar to the previously discussed stress field. The maximum shear stress (1–1.4 GPa) is concentrated inside the bottom part of the metastable wedge of the α to $\alpha + \gamma$ phase transition in the depth range 380–430 km and along the phase boundaries of $\alpha + \gamma$ to β and β to γ in the depth range 380–450 km; thus two layers of high shear stress exist. High shear stress is also found

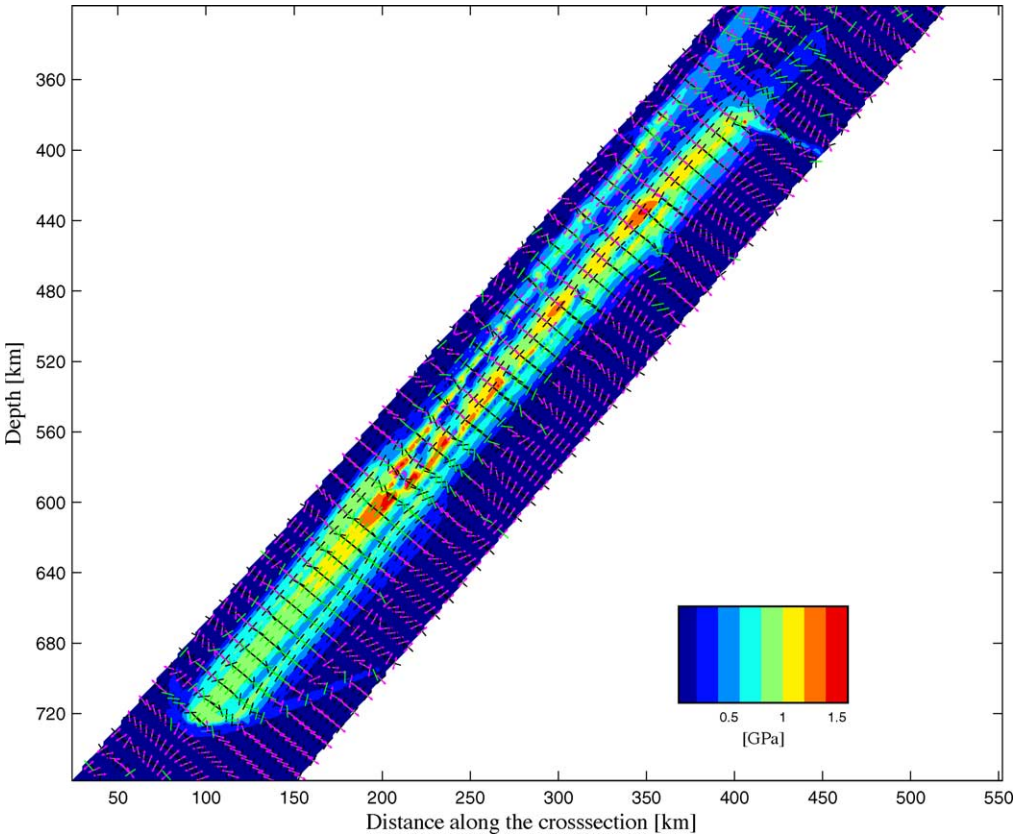

Fig. 4. Distribution of shear stress and orientation of principal stress axes in the subducting slab. The 'cold' mantle temperature profile was used to determine the temperature inside the slab. The color scale represents the magnitude of shear stress. The orientation of the principal stress axis is shown by colored dashes; black, green and magenta dashes show the orientation of compression, middle axis, and tension, respectively. The orientation of the principal stress axis that is parallel to the trench is not plotted.

below the β to γ phase transition and in the depth range around 450–640 km (Figs. 6 and 7).

The state of stress in the depth range 380–430 km is different in the two layers. In the upper layer, tension is in the plane of the slab, and compression is perpendicular to the slab plane. In the lower layer, the highest shear stress is inside the metastable wedge, where compression is in a down-dip direction, the middle axis is trench parallel and tension is perpendicular to the slab plane. High shear stress is also concentrated along the metastable phase boundary (Figs. 6 and 7), where compression is perpendicular to the slab plane, the middle axis is oriented down-dip and tension is parallel to the trench. Below 430 km depth, high shear stress is related to the β to γ phase transition. In the depth range 430–440 km, compression is perpendicular to the slab plane, the middle axis is in a down-dip direction, and tension is trench parallel. The state of stress is occurring in the region where β transforms to the γ phase. Below 440 km depth, where the β to γ equilibrium phase transition is completed, compression is in a down-dip direction, the middle axis is perpendicular to the slab plane, and tension is parallel to the trench in both layers. The shear stress associated with the equilibrium phase transitions is caused by the non-uniform distribution of viscosity across the slab Slancova et al. (2002). The central cold part of the slab is stiffer than the warmer boundary which is more contracted and causes stresses in the central cold part. The shear stress in the central part of the slab is relaxed due to the low viscosity caused by grain size reduction (Fig. 7) and only two stripes of down-dip compression

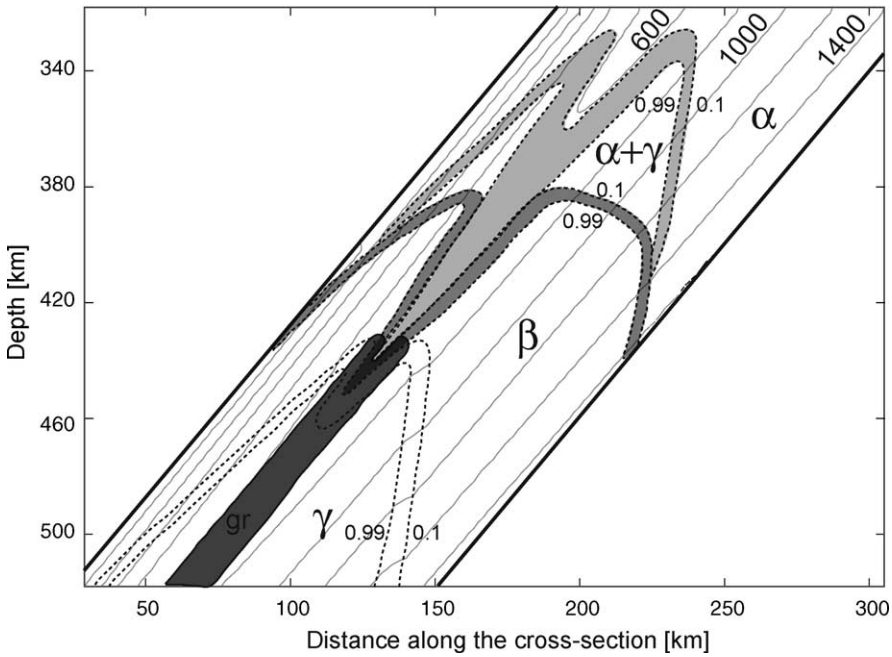

Fig. 5. Temperature (K) distribution (gray solid lines), phase boundaries (dashed lines), and the area of grain size reduction (gray filled area, labeled 'gr', and defined by solid black lines) in the subducting slab. The 'hot' mantle temperature profile was used to determine the temperature distribution inside the slab. Degrees of transformation 0.1 and 0.99 are shown.

persist on both sides of the area with reduced grain size. The strip of the high shear stress near the center of the slab at 500 km depth decreases in magnitude to the depth of the γ to perovskite + magnesiowüstite phase transition, where its magnitude is about 500 MPa. The stress below the γ to perovskite + magnesiowüstite phase transition is fully relaxed.

The reason the shear stress below the metastable wedge is relaxed for the 'hot' temperature model and not relaxed for the 'cold' temperature model, is the pressure dependence of the rheological law. The grain sizes are very similar in both models and phase transitions occur along a similar temperature isoline, but the wedge of the metastable olivine extends to greater depths (and hence to higher pressure) in the 'cold' model than in the 'hot' model.

4. Discussion

The volume reductions due to the metastable phase transitions cause a stress field that can be responsible for the double seismic zones observed in the Tonga subduction zone. A double layer of high shear stress aligns along the phase boundaries. The upper layer can be characterized as in-plane tensional with either the tension or middle axis oriented down-dip. This agrees with observations of stress during earthquakes (events 1–4, especially 2 and 3, Fig. 8) where focal mechanisms in the upper layer show in-plane tension (Wiens et al., 1993). The stress in the lower layer in our model is down-dip compressional with tension perpendicular to the slab plane, in agreement with earthquake focal mechanisms (events 5–7, especially 5 and 6, Fig. 8). We also obtained compression perpendicular to the slab plane, which is not observed in the lower seismic layer. A similar state of stress was found by Devaux et al. (2000). Since the shear stress is slightly lower than in the upper layer, the model predicts that the upper layer should be less seismically active than the lower layer. When the 'hot' mantle temperature profile is used, the double zone of high shear stress lies between 380 and 440 km depth in perfect agreement with the depth range of the double seismic zone in Tonga. The upper depth limit of the double layer is determined by the depth location of the α to β phase

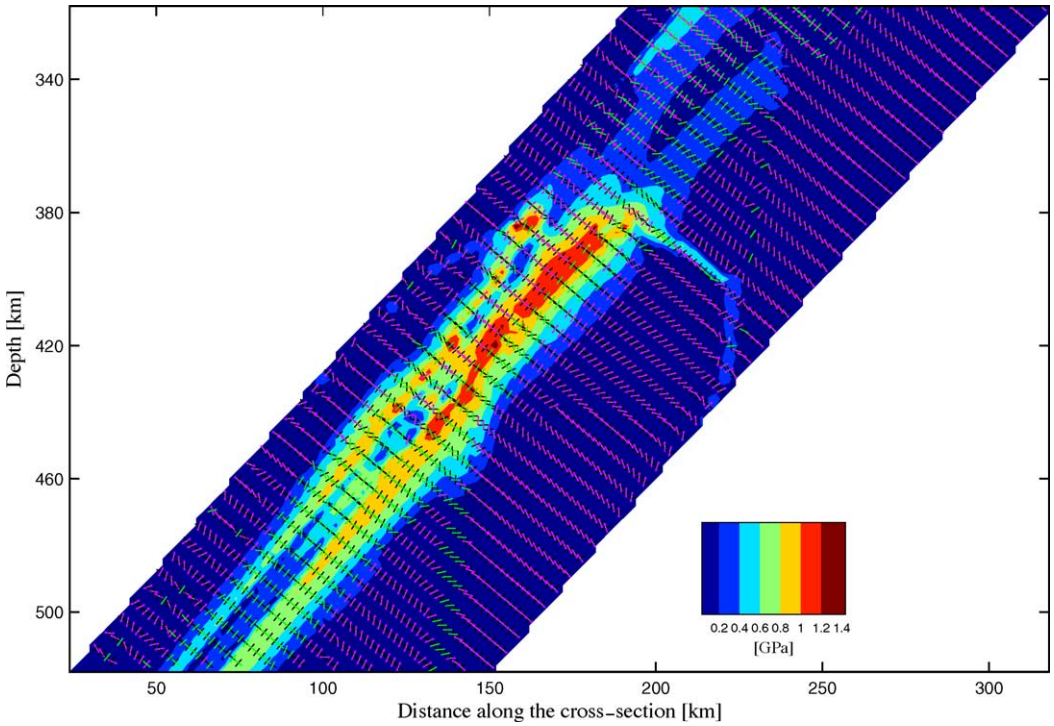

Fig. 6. Distribution of shear stress and orientation of principal stress axes in the subducting slab. The 'hot' mantle temperature profile was used to determine the temperature inside the slab. The color scale represents the magnitude of shear stress. The orientation of the principal stress axis is shown by colored dashes; black, green and magenta dashes show the orientation of compression, middle axis, and tension, respectively. The orientation of the principal stress axis that is parallel to the trench is not plotted.

transition. Our idea is to explain the occurrence of a double seismic zone by shearing along a metastable wedge. Since the double seismic zone of Izu-Bonin (300–400 km) and Tonga (350–420 and 380–460 km) occur at different depths, we need an explanation of why the metastable wedge would be located at different depths. The deeper end of a metastable wedge can be easily explained by the temperature difference in the subducting slab, because the transformation rate of the new phase is strongly temperature dependent. The temperature inside the slab can be changed by changing the thickness of the slab, the lithospheric basal temperature or the mantle temperature profile, parameters that are not precisely known for an individual subduction zone. However, the upper end of the metastable wedge is more problematic. A change in the mantle temperature profile by 200 K does not move the upper end of the metastable wedge to a different depth, but moves it across the slab (horizontally, see Figs. 3 and 5). The depth difference between the upper ends of the double seismic zones in Tonga and Izu-Bonin is 50–80 km. This depth difference corresponds to a pressure difference of about 1.5 GPa. Taking into account the Clapeyron slope of the α to β phase transformation, a change in pressure of 1.5 GPa corresponds to a change in temperature of 943 K. This is too high a temperature difference; the two subduction zones would differ at depths of around 350 km. The presence of 10% of Fe in the chemical composition of olivine shifts the phase transformation by 1.5 GPa to a lower depth that seems to be more suitable explanation for the observations of the double seismic zones at different depths based on our analysis.

If stress is released by transformational faulting, failure occurs for degrees of transformation around 10% (Burnley et al., 1991), and stresses would be characterized by down-dip compression in the lower layer. Variations in the degree of transformation required for failure may be responsible for the fact that the double

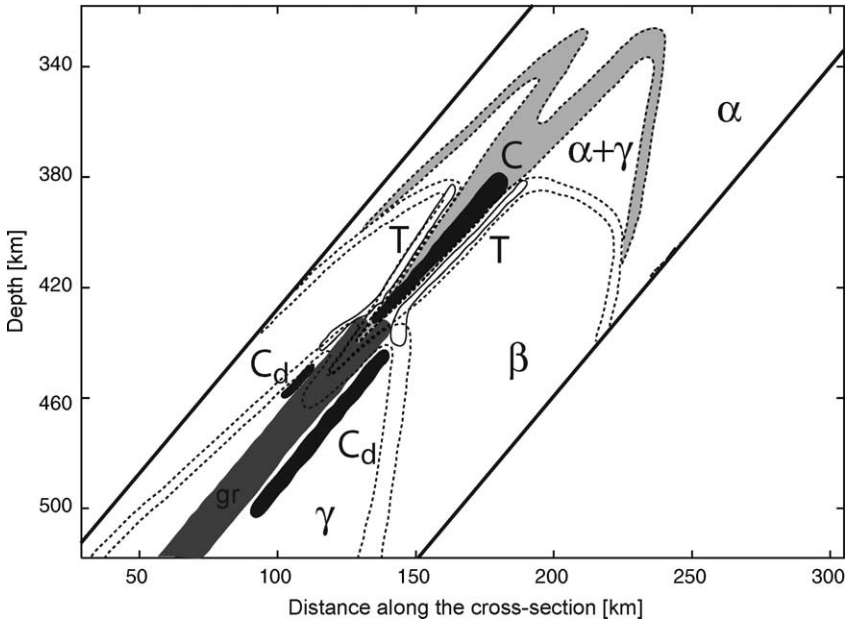

Fig. 7. Sketch of areas of high shear stress (black filled and transparent ovals) and their relation to the phase boundaries (dotted lines). '*C*' denotes a down-dip compression in the metastable wedge, 'C_d' denotes a down-dip compression below the equilibrium phase transition, and '*T*' denotes the in-plane tension along the phase boundaries. The area of grain size reduction is gray filled, labeled 'gr', and defined by solid black lines. Degrees of transformation 0.1 and 0.99 are shown. The same temperature model as in Figs. 5 and 6 is used.

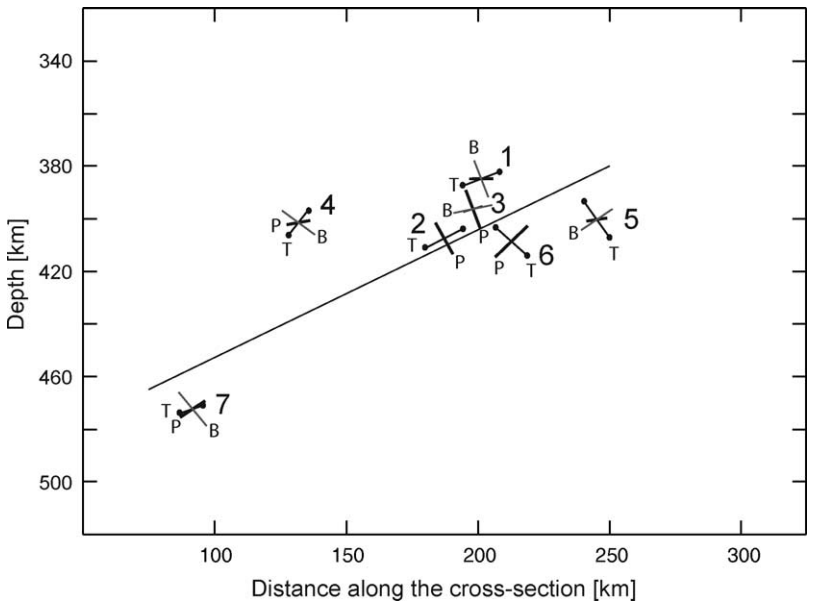

Fig. 8. Orientation of *P* (thick dashes), *B* (thin dashes) and *T* (dashes with balls) axes in the Tonga double seismic zone projected on the plane of the cross-section. Data are taken from Wiens et al. (1993) and depicted in the same way.

seismic layer is observed only in some parts of the Wadati–Benioff zones.

Model shear stresses seem to be too high in comparison with the assumed strength of the lithosphere (Davies, 1980). Kanamori et al. (1998) report a stress drop of 70 MPa during the deep Bolivia earthquake in 1994, but they also show that the efficiency of deep earthquakes is low, implying that the magnitude of stress drop in the slab must be significantly smaller than the magnitude of the shear stress in the slab. The modeled magnitude of the shear stress is dependent on the volumetric strain ϵ_{ij}^{V} and viscosity. Since the magnitude of volumetric strain is determined by density, only a slower nucleation-growth rate could decrease the degree of phase transformation during a time step and thus the magnitude of shear stress. Another way to decrease the magnitude of shear stress is through the rheological law, for example, by considering complex mineralogy, water content, etc. A coupled thermo-mechanical solution would cause a slower nucleation-growth rate through pressure drop during the phase transformation. Alternatively, shear heating would increase this rate and thus sharpen the phase boundary (a detailed discussion about the modeled magnitude of shear stress below equilibrium phase boundaries is given in Slancova et al., 2002).

There are some important forces acting on the slab that are not considered in this paper. One is the buoyancy force which was studied by Goto et al. (1985), Bina (1997), Yoshioka et al. (1997), and Devaux et al. (2000). Devaux et al. (2000) showed that stresses due to buoyancy forces are of the order of a hundred MPa. Another force that was not considered is the resistance force arising from the interaction of the slab with the mantle (Yoshioka and Wortel, 1995; Vassiliou and Hager, 1988). The effect of this force is of the order of a hundred MPa. Since shear stresses due to the volume changes during phase transformations are significantly higher (about 500–1000 MPa), these other forces seem to be negligible. However, if the phase change associated this stress would be decreased by physical effects not accounted for in the numerical model, then these forces may become important.

The metastable wedge in numerical models does not reach the depth of the deepest earthquakes in Tonga even with use of the coldest possible temperature inside the slab (Devaux et al., 2000), so transformational faulting associated with metastability does not explain all deep seismic activity in Tonga (it is based on the assumption that 10 cm per year is a high subduction velocity). In the model with a 'hot' mantle temperature profile, the state of stress changes its character immediately below the metastable wedge. Compression stays oriented down-dip, but tension perpendicular to the slab plane changes its orientation to the direction along the trench at a depth of around 440 km (Fig. 6). This agrees with the general character of Tonga seismic activity from HCMT solutions (Jiao et al., 2000), where the P axes are oriented down-dip throughout the slab, but B axes are trench parallel and T axes are perpendicular to the slab plane down to 450 km depth, while below 450 km depth the B and T axes become interchanged. Even though our model fits only the T axes oriented along the trench, it represents the seismic activity in the Tonga subduction zone fairly well.

Our model supports the idea of several possible stress release mechanisms for deep earthquakes (e.g., Houston et al., 1998). In the depth range of about 300–450 km, transformational faulting may be the active failure mechanism, whereas deeper than 450 km, another mechanism for deep earthquakes, e.g., dehydration embrittlement, thermal shear instability, ductile faulting, or crystallographic shear not associated with metastability of olivine (e.g., Kirby et al., 1996) may release the stress.

5. Conclusions

A double layer of high shear stress arises along the metastable olivine wedge in the depth range 350–460 km. The state of stress in the upper layer is in-plane tension and the stress state in the lower layer is down-dip compression. The modeled stress field agrees with the stress observed in the Tonga double seismic zone.

High shear stress also arises at depths below the metastable wedge. It is characterized by down-dip compression and trench-parallel tension, in agreement with some of the focal mechanisms deep in the Tonga subduction zone. The model suggests that at least two stress release mechanisms for deep earthquakes may act in the Tonga subducting slab. One, transformational faulting, is restricted to the metastable wedge and the other, not specified, acts below the metastable wedge.

Acknowledgements

We thank S. Yoshioka and one anonymous reviewer for their helpful reviews. Supported by a grant from the Los Alamos Institute of Geophysics and Planetary Physics.

References

Akaogi, M., Navrotsky, A., Yagi, T., Akimoto, S., 1987. Pyroxene-garnet transition: thermochemistry and elasticity of garnet solid solutions, and application to a pyrolite mantle. In: Manghnani, M.H., Syono, Y. (Eds.), High-Pressure Research in Mineral Physics. Am. Geophys. Union Geophys. Monogr. Ser. 39, pp. 251–260.

Akaogi, M.E., Ito, E., Navrotsky, A., 1989. Olivine-modified spinel transitions in system Mg_2SiO_4–Fe_2SiO_4: calorimetric measurements, thermomechanical calculations, and geophysical implications. J. Geophys. Res. 94, 15,671–15,685.

Anderson, O.L., Isaak, D.G., 1995. Elastic constants of mantle minerals at high temperature. In: Ahrens, T.J. (Ed.), Mineral Physics and Crystallography: A Handbook of Physical Constants. Am. Geophys. Union, pp. 64–97.

Bina, C.R., 1996. Phase transition buoyancy contributions to stresses in subducting lithosphere. Geophys. Res. Lett. 23, 3563–3566.

Bina, C.R., 1997. Patterns of deep seismicity reflect buoyancy stresses due to phase transition. Geophys. Res. Lett. 24, 3301–3304.

Brudzinski, M.R., Chen, W.-P., 2000. Variations in P wave speeds and outboard earthquakes: Evidence for a petrologic anomaly in the mantle transition zone. J. Geophys. Res. 105, 21661–21682.

Burnley, P.C., Green, H.W., Prior, D.J., 1991. Faulting associated with the olivine to spinel transformation in Mg_2GeO_4 and its implications for deep-focus earthquakes. J. Geophys. Res. 96, 425–443.

Cahn, J.W., 1956. The kinetics of grain boundary nucleated reactions. Acta Metall. 4, 449–459.

Chen, W.-P., Brudzinski, M.R., 2001. Evidence for a large-scale remnant of subducted lithosphere beneath Fiji. Science 292, 2475–2479.

Collier, J.D., Helffirch, G.R., Wood, B.J., 2001. Seismic discontinuities and subduction zones. Phys. Earth Planet. Inter. 127, 35–49.

Daessler, R., Yuen, D.A., Karato, S., Riedel, M.R., 1996. Two-dimensional thermo-kinetic model for the olivine-spinel phase transition in subducting slabs. Phys. Earth Planet. Inter. 94, 217–239.

Devaux, J.P., Schubert, G., Anderson, C., 1997. Formation of a metastable olivine wedge in a descending slab. J. Geophys. Res. 102, 24,627–24,637.

Devaux, J.P., Fleitout, L., Schubert, G., 2000. Stresses in a subducting slab in the presence of a metastable olivine wedge. J. Geophys. Res. 105, 13,365–13,373.

Davies, G.F., 1980. Mechanics of subducted lithosphere. J. Geophys. Res. 85, 6304–6318.

Duffy, T.S., Anderson, D.L., 1989. Seismic velocities in mantle minerals and the mineralogy of the upper mantle. J. Geophys. Res. 94, 1,895–1,912.

Dziewonski, A.M., Anderson, D.L., 1981. Preliminary reference Earth model (PREM). Phys. Earth Planet. Inter. 25, 297–356.

Frost, H.J., Ashby, M.F., 1982. Deformation-mechanism Maps. Pergamon Press, Oxford, 168 pp.

Goetze, C., Evans, B., 1979. Stress and temperature in the bending lithosphere as constrained by experimental rock mechanics. Geophys. J. R. Astron. Soc. 59, 463–478.

Goto, K., Hamaguchi, H., Suzuki, Z., 1983. Distribution of stress in descending plate in special reference to intermediate and deep focus earthquakes. I. Characteristics of thermal stress distribution. Tôhoku Geophys. J. 29, 81–105.

Goto, K., Hamaguchi, H., Suzuki, Z., 1985. Earthquake generating stresses in a descending slab. Tectonophysics 112, 111–128.

Goto, K., Suzuki, Z., Hamaguchi, H., 1987. Stress distribution due to olivine-spinel phase transition in descending plate and deep focus earthquakes. J. Geophys. Res. 92, 13811–13820.

Green II, H.W., Burnley, P.C., 1989. A new self-organizing mechanism for deep-focus earthquakes. Nature 341, 733–737.

Guest, A., Schubert, G., Gable, C., 2003. Stress field in the subducting lithosphere and comparison with deep earthquakes in Tonga. J. Geophys. Res. 108, 2288.

Houston, H., Benz, H.M., Vidale, J., 1998. Time functions of deep earthquakes from broadband and short-period stacks. J. Geophys. Res. 103, 29,895–29,914.

Iidaka, T., Suetsugu, D., 1992. Seismological evidence for metastable olivine inside a subducting slab. Nature 356, 593–595.

Iidaka, T., Furukawa, Y., 1994. Double seismic zone for deep earthquakes in the Izu-Bonin subduction zone. Science 263, 1116–1118.

Iidaka, T., Obara, K., 1997. Seismological evidence for the existence of anisotropic zone in the metastable wedge inside the subducting Izu-Bonin slab. Geophys. Res. Lett. 24, 3305–3308.

Jeanloz, R., Thompson, A.B., 1983. Phase transitions and mantle discontinuities. Rev. Geophys. 21, 51–74.

Jiao, W., Silver, P.G., Fei, Y., Prewitt, C.T., 2000. Do intermediate- and deep-focus earthquakes occur on preexisting weak zones? An examination of the Tonga subduction zone. J. Geophys. Res. 105, 28125–28138.

Kanamori, H.D., Anderson, D.L., Heaton, T.H., 1998. Frictional melting during the rupture of the 1994 Bolivian earthquake. Science 279, 839–842.

Karato, S., Riedel, M.R., Yuen, D.A., 2001. Rheological structure and deformation of subducted slabs in the mantle transition zone: implications for mantle circulation and deep earthquakes. Phys. Earth Planet. Inter. 127, 83–108.

Kirby, S.H., Durham, W.B., Stern, L.A., 1991. Mantle phase changes and deep-earthquake faulting in subducting lithosphere. Science 252, 216–225.

Kirby, S.H., Stein, S., Okal, E., Rubie, D.C., 1996. Metastable mantle phase transformations and deep earthquakes in subducting oceanic lithosphere. Rev. Geophys. 34, 261–306.

Koper, K.D., Wiens, D.A., Dorman, L.M., Hildebrand, J.A., Webb, S.C., 1998. Modeling the Tonga slab: can travel time data resolve a metastable olivine wedge? J. Geophys. Res. 103, 30079–30100.

Madariaga, R., 1976. Dynamics of an expanding circular fault. Bull. Seism. Soc. Am. 66, 163–182.

Presnell, D.C., Walter, J., 1993. Melting of forsterite, Mg_2SiO_4, from 9.7 to 16.5 GPa. J. Geophys. Res. 98, 19,777–19,783.

Riedel, M.R., Karato, S., 1996. Microstructural development during nucleation and growth. Geophys. J. Int. 125, 397–414.

Riedel, M.R., Karato, S., 1997. Grain-size evolution in subducted oceanic lithosphere associated with the olivine-spinel transformation and its effects on rheology. Earth Planet. Sci. Lett. 148, 27–43.

Ringwood, A.E., 1982. Phase transformations and differentiation in subducted lithosphere: Implications for mantle dynamics, basalt petrogenesis, and crustal evolution. J. Geol. 90, 611–643.

Rubie, D.C., Ross II, C.R., 1994. Kinetics of the olivine-spinel transformation in subducting lithosphere: experimental constraints and implications for deep slab processes. Phys. Earth Planet. Inter. 86, 223–241.

Sawamoto, H., Weidner, D.J., Sasaki, S., Kumazawa, M., 1984. Single-crystal elastic properties of the modified spinel (beta) phase of magnesium orthosilicate. Science 224, 749–751.

Stein, C.A., Stein, S.S., 1992. A model for the global variation in oceanic depth and heat flow with lithospheric age. Nature 359, 123–129.

Stixrude, L., Hemley, R.J., Fei, Y., Mao, H.K., 1992. Thermoelasticity of silicate perovskite and magnesiowüstite and stratification of the Earth's mantle. Science 257, 1099–1101.

Turcotte, D.L., Schubert, G., 1982. Geodynamics. Wiley, New York.

Vassiliou, M.S., Hager, B.H., 1988. Subduction zone earthquakes and stress in slabs. Pure Appl. Geophys. 128, 574–624.

Wang, Z., Karato, S.-I., Fujino, K., 1993. High temperature creep of single crystal strontium titanate ($SrTiO_3$): a contribution to creep systematics in perovskite. Phys. Earth Planet. Inter. 79, 299–312.

Wang, Z.W., 1999. The melting of Al-bearing perovskite at the core-mantle boundary. Phys. Earth Planet. Inter. 115, 219–228.

Weidner, D.J., Sawamoto, H., Sasaki, S., 1984. Single-crystal elastic properties of the spinel phase of Mg_2SiO_4. J. Geophys. Res. 89, 7852–7859.

Wiens, D.A., McGuire, J.J., Shore, P.J., 1993. Evidence for transformational faulting from a deep double seismic zone in Tonga. Nature 364, 790–793.

Wright, K., Price, G.D., Poirier, J.-P., 1992. High-temperature creep of the perovskites $CaTiO_3$ and $NaNbO_3$. Phys. Earth Planet. Inter. 74, 9–22.

Yeganeh-Haeri, A., Weidner, D.J., Ito, E., 1989. Elasticity of $MgSiO_3$ in the perovskite structure. Science 243, 787–789.

Yoshioka, S., Wortel, M.J.R., 1995. Three-dimensional numerical modeling of detachment of subducted lithosphere. J. Geophys. Res. 100, 20,223–20,244.

Yoshioka, S., Daessler, R., Yuen, D.A., 1997. Stress fields associated with metastable phase transitions in descending slabs and deep-focus earthquakes. Phys. Earth Planet. Inter. 104, 345–361.

Yusa, H., Akaogi, M., Ito, E., 1993. Calorimetric study of $MgSiO_3$ garnet and pyroxene: Heat capacities, transition enthalpies, and equilibrium phase relations in $MgSiO_3$ at high pressures and temperatures. J. Geophys. Res. 98, 6453–6460.

Zerr, A., Boehler, R., 1994. Constraints on the melting temperature of the lower mantle from high-pressure experiments on MgO and magnesiowüstite. Nature 371, 506–508.